LUND UNIVERSITY

Smoothness-constrained time-lapse inversion of data from 3D resistivity surveys

Loke, M. H.; Dahlin, Torleif; Rucker, D. F.

Link to publication

Total number of authors:
3

Smoothness-constrained time-lapse inversion of data from 3D resistivity surveys

M.H. Loke[1*], T. Dahlin[2] and D. F. Rucker[3]

[1] *Geotomo Software, 115 Cangkat Minden Jalan 6, 11700 Gelugor, Penang, Malaysia*

[2] *Lund University Engineering Geology, Lund University, John Ericssons väg 1, S-223 63 Lund, Sweden*

[3] *hydroGEOPHYSICS, Inc., 2302 N. Forbes Blvd., Tucson, AZ 85745, USA*

ABSTRACT

Three-dimensional resistivity surveys and their associated inversion models are required to accurately resolve structures exhibiting very complex geology. In the same light, 3D resistivity surveys collected at multiple times are required to resolve temporally varying conditions. In this work we present 3D data sets, both synthetic and real, collected at different times. The large spatio-temporal data sets are then inverted simultaneously using a least-squares methodology that incorporates roughness filters in both the space and time domains. The spatial roughness filter constrains the model resistivity to vary smoothly in the x-, y- and z-directions. A temporal roughness filter is also applied that minimizes changes in the resistivity between successive temporal inversion models and the L-curve method is used to determine the optimum weights for both spatial and temporal roughness filters. We show that the use of the temporal roughness filter can accurately resolve changes in the resistivity even in the presence of noise. The L1- and L2-norm constraints for the temporal roughness filter are first examined using a synthetic model. The synthetic data test shows that the L1-norm temporal constraint produces significantly more accurate results when the resistivity changes abruptly with time. The model obtained with the L1-norm temporal constraint is also less sensitive to random noise compared with independent inversions (i.e., without any temporal constraint) and the L2-norm temporal constraint. Anomalies that are common in models using independent inversions and the L2-norm and L1-norm temporal constraints are likely to be real. In contrast, anomalies present in a model using independent inversions but that are significantly reduced with the L2-norm and L1-norm constraints are likely artefacts. For field data sets, the method successfully recovered temporal changes in the subsurface resistivity from a landfill monitoring survey due to rainwater infiltration, as well as from an experiment to map the migration of sodium cyanide solution from an injection well using surface and borehole electrodes in an area with significant topography.

INTRODUCTION

Over the last 15 years, the application of two-dimensional (2D) resistivity surveys has become one of the standard geophysical methods used to map areas with moderately complex geology (Loke *et al.* 2011). However, in very complex areas, the 2D inversion model can suffer from artefacts due to structures on the periphery of the survey line (Bentley and Gharibi 2004; Johansson *et al.* 2007). To overcome the off-line effects, a three-dimensional (3D) survey and inversion model may be required to obtain sufficiently accurate results (Dahlin *et al.* 2002; Wilkinson *et al.* 2006; Legault *et al.* 2008). Three-dimensional surveys using electrodes on the ground surface as well as in boreholes are now becoming more practical due to recent advances in multi-

channel instrumentation, field methodology, data inversion algorithms and microcomputer technology (Gharibi and Bentley 2005; Chambers *et al.* 2006; Loke 2011).

In some areas, repeated 3D surveys are carried out to detect temporal changes of the subsurface (Rosqvist *et al.* 2010) and to more fully understand movement of fluids and contaminants in soil and groundwater (Singha and Gorelick 2006; Oldenborger *et al.* 2007; Hayley *et al.* 2009; Rucker *et al.* 2011). Previous attempts to accommodate time-lapse resistivity in inverse models have been to invert each snapshot independently (Cassiani *et al.* 2006), invert the resistivity difference between snapshots (Labreque and Yang 2001), invert the ratio of initial and subsequent snapshots (Daily *et al.* 1992), simultaneous inversion (Hayley *et al.* 2011) and incorporating the temporal data and model directly into the least-squares regularization method (Kim *et al.* 2009).

* drmhloke@yahoo.com

In recent years, automatic data acquisition systems have become increasingly sophisticated (Ogilvy *et al.* 2009; Rucker *et al.* 2012). These systems are often used in complex geological environments, such as landslide zones, dams and landfills where 2D models can suffer from artefacts due to off-line structures. Thus a fully 3D model is crucial (Bentley and Gharibi 2004). The systems produce large volumes of data, frequently on a daily basis, where rapid interpretation is important. Our interest in ameliorating this problem, as demonstrated below, is in developing stable and robust time-lapse inversion techniques for 3D models that can be incorporated into automatic inversion software to produce images that are reasonably free of artefacts and provide interpretable results when used by field staff who might not be familiar with the inversion theory. The 4D inversion method by Kim *et al.* (2009, 2010) was modified for 3D space models and to incorporate the L-curve method (Farquharson and Oldenburg 2004) to determine the optimum spatial and temporal damping factors.

Towards this goal, the paper has been organized such that the following section gives a brief theoretical description of the inversion algorithms used, followed by results from tests with a synthetic data set. Finally, examples from two field surveys are presented that show (1) the movement of water and methane gas in a landfill site and (2) an experiment to monitor the movement of a barren sodium cyanide solution from a gold mine heap where electrodes are placed both on the surface and in boreholes.

THEORY

The constrained least-squares optimization method

The smoothness-constrained least-squares optimization method is frequently used for both 2D and 3D inversion of resistivity data (Loke *et al.* 2003), with the objective to minimize the difference between modelled and measured data. The optimization equation that gives the relationship between model parameters and measured data (Farquharson and Oldenburg 1998) is:

$$\left[\mathbf{J}_i^T \mathbf{R}_d \mathbf{J}_i + \lambda_i \mathbf{W}^T \mathbf{R}_m \mathbf{W}\right] \Delta \mathbf{r}_i = \mathbf{J}_i^T \mathbf{R}_d \mathbf{g}_i - \lambda_i \mathbf{W}^T \mathbf{R}_m \mathbf{W} \mathbf{r}_{i-1}. \qquad (1)$$

In equation (1), the Jacobian matrix $\mathbf{J}$ contains the sensitivities of the measurements with respect to the model parameters, λ is the damping factor vector and $\mathbf{g}$ is the data misfit vector. $\mathbf{r}_{i-1}$ is the model parameter vector (the logarithm of the model resistivity values) for the previous iteration, while $\Delta \mathbf{r}_i$ is the change in the model parameters. $\mathbf{W}$ incorporates the roughness filters in the x-, y- and z- directions. $\mathbf{R}_d$ and $\mathbf{R}_m$ are weighting matrices introduced so that different elements of the data misfit and model roughness vectors are given equal weights if the L1-norm inversion method is used (Farquharson and Oldenburg 1998; Loke *et al.* 2003). Figure 1 shows a simple division of the subsurface into rectangular model cells (Loke and Barker 1996), where the corners of cells in the x- and y-directions follow the positions of the electrodes on the surface arranged in a rectangular grid. Recent developments have allowed more complex models where the electrodes need not be arranged in a rectangular grid (Rucker *et al.* 2010; Rucker and Noonan 2013). The roughness filter couples the resistivity of each model cell with the neighbouring cells (Fig. 2). The roughness filter is usually applied in the horizontal and vertical directions only. However, in some situations, better results can be obtained by incorporating diagonal filter components as well (Farquharson 2008; Loke and Dahlin 2010).

A comparison of different time-lapse inversion techniques is given by Hayley *et al.* (2011). Our preference is the 4D inversion methodology by Kim *et al.* (2009) that directly incorporates the time domain with the space domain. It is proven to be a stable and robust technique reasonably free of artefacts compared to some other techniques and has the advantage that it can be modified to account for changes that occur within a measurement cycle (Hayley *et al.* 2011). Thus, our implementation of the time-lapse inversion technique uses the following equation:
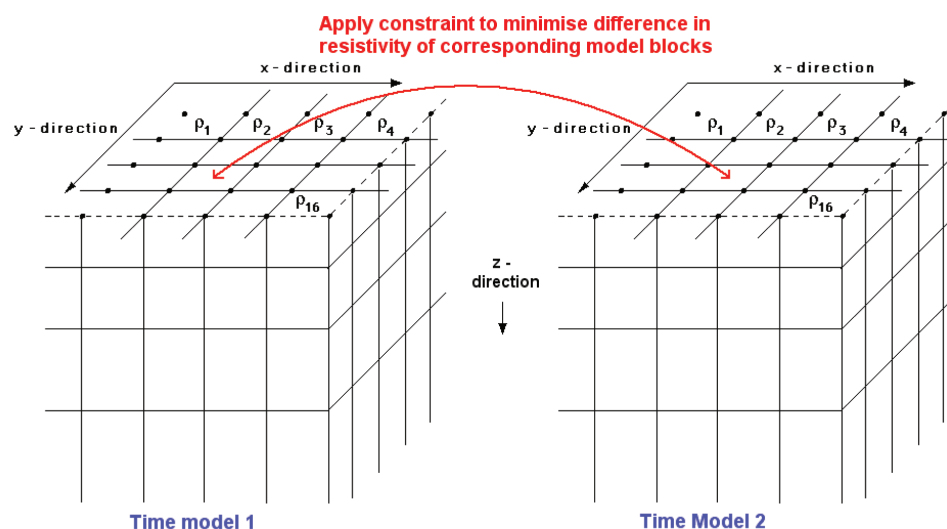

FIGURE 1

Schematic diagram of the 3D model used for the survey with a rectangular grid of electrodes and the use of a cross-model time-lapse smoothness constraint.
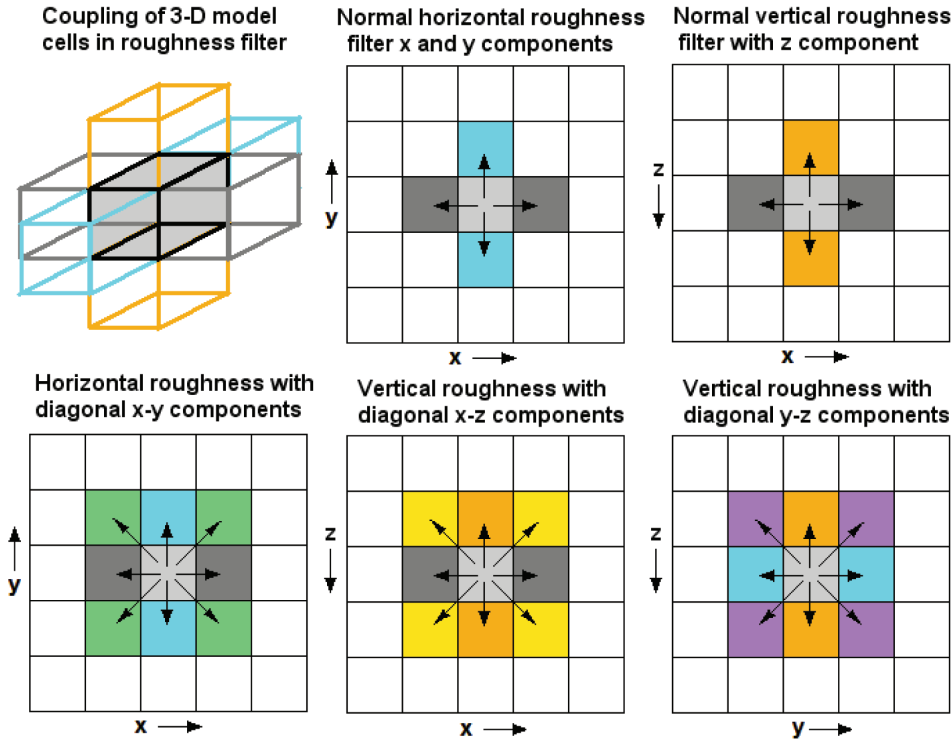
Coupling of 3-D model cells in roughness filter

Normal horizontal roughness filter x and y components

Normal vertical roughness filter with z component

Horizontal roughness with diagonal x-y components

Vertical roughness with diagonal x-z components

Vertical roughness with diagonal y-z components

FIGURE 2
Types of roughness filters used to minimize resistivity changes between neighbouring model cells.

$$\left[\mathbf{J}_i^T\mathbf{R}_d\mathbf{J}_i + \left(\lambda_i\mathbf{W}^T\mathbf{R}_m\mathbf{W} + \alpha_i\mathbf{M}^T\mathbf{R}_t\mathbf{M}\right)\right]\Delta\mathbf{r}_i =$$

$$\mathbf{J}_i^T\mathbf{R}_d\mathbf{g}_i - \left(\lambda_i\mathbf{W}^T\mathbf{R}_m\mathbf{W} + \alpha_i\mathbf{M}^T\mathbf{R}_t\mathbf{M}\right)\mathbf{r}_{i-1} \quad (2)$$

where $\mathbf{M}$ is the difference matrix applied across the time models with only the diagonal and one sub diagonal elements having values of 1 and –1, respectively. Equation (2) aims to minimize the difference in the resistivity of each model cell and the corresponding cell for the next temporal model, or snapshot (Fig. 1). Equation (2) is slightly different from that used in Kim *et al.* (2009) as it incorporates the $\lambda_i\mathbf{W}^T\mathbf{R}_m\mathbf{W}$ term in the right-hand side to ensure that the roughness filter is applied directly on the model parameters $\mathbf{r}_i$ as well as on the parameter change vector $\Delta\mathbf{r}_i$ where $\mathbf{r}_i = \mathbf{r}_{i-1} + \Delta\mathbf{r}_i$. α is the temporal damping factor that gives the relative weight for minimizing the temporal changes in the resistivity compared to the model roughness and data misfit. Higher values of α will result in time-lapsed inverted models that are more similar to one another at the expense of a higher data misfit (Rucker *et al.* 2011). $\mathbf{R}_t$ is a weighting matrix used by the L1- or L2-norm method for the temporal constraint and is equal to the identity matrix $\mathbf{I}$ if the L2-norm temporal constraint is used (Kim *et al.* 2009). The L2-norm constraint minimizes the sum of the squares of the change in the resistivity between adjacent temporal models. To implement the L1-norm temporal constraint, we use the iterative reweighed least-squares method (Farquharson and Oldenburg 1998). The L1-norm constraint minimizes the sum of the absolute value of the temporal changes in the resistivity. The L1-norm temporal constraint is shown by

Kim *et al.* (2010) to significantly improve the results for some 2D time-lapse models.

The model vector $\mathbf{r}$ in equation (2) now contains the resistivity of all the different temporal models. If the model has n model cells and there are t snapshots, $\mathbf{r}$ will have nt model parameters. Similarly the data misfit vector $\mathbf{g}$ will have mt components if each snapshot has m data points. We use an iterative method based on the linear-conjugate gradient method (Li and Oldenburg 1996) to solve the least-squares formulation in equation (2). The Jacobian matrix has a very sparse structure, as demonstrated in Fig. 3, with only nmt non-zero elements. This sparse structure can be efficiently exploited by the linear-conjugate gradient method such that mathematical operations are only carried out on the non-zero elements of the matrix. In our implementation, it is assumed that the resistivity does not change significantly during the time taken to measure a single data set. However the resistivity of the model is allowed to vary in a non-linear fashion between the first and last snapshots.

For areas where the topography is not significant, the resistivity model uses the finite-difference method to calculate the apparent resistivity values, as well as the associated Jacobian matrix (Dey and Morrison 1979; Loke and Barker 1996; Spietzer *et al.* 1999; Rucker *et al.* 2009). The finite-element method (Holcombe and Jiracek 1984; Sasaki 1994; Zhou and Greenhalgh 2001; Marescot *et al.* 2008) is used in areas with significant topography. The Jacobian matrix values are recalculated after each iteration with the adjoint-equation approach using the potential values at the nodes of the mesh due to a current source

for each electrode position (McGillivray and Oldenburg 1990; Sasaki 1994). The details on the calculation of the potential values and the Jacobian matrix can be found in these references.

Use of the L-curve method to determine the optimum damping factors

Spatial and temporal damping factors play an important role in determining the final model obtained from the inversion process. The optimum values depend on the noise characteristics of the data set and the degree to which the temporal resistivity variations compare to the spatial variations. As an example, Hayley *et*
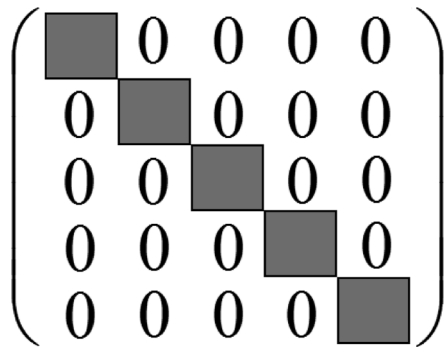
FIGURE 3

Example of a Jacobian matrix structure for five time-series data sets and models. Each grey rectangle represents the Jacobian matrix associated with a single set of measurements.

al. (2011) carried out repeated inversions with different values of the temporal damping factor to determine the value that produces results more closely related to a known structure for a synthetic data set. Manually adjusting the damping factor is impractical for 3D field surveys due to the long inversion times. Additionally, the lack of sufficiently accurate information to distinguish artefacts from true structures at most field sites prevents the practitioner from knowing if the optimal damping factor has been chosen. Therefore, efficient automatic inversion software requires an adaptive technique to determine the optimum damping factors for data sets of differing data quality measured over areas with arbitrary resistivity contrasts in both space and time.

If the noise level is known, such as from reciprocal measurements, a cooling-schedule-type method to select the appropriate value of the spatial damping factor λ can be used (Farquharson and Oldenburg 2004). A large value of λ, usually in the range of about 0.10–0.20, is initially used and is reduced by half after each iteration until it reaches a preset minimum value (usually about one-tenth to one-twentieth the initial value). The model that has a data misfit similar to the noise level is then selected.

Tests with a number of different data sets can provide a plausible range of values for the spatial and temporal damping factors. These values can then be refined by automatic techniques to determine the optimum damping factors that suit the data set. Farquharson and Oldenburg (2004) provided a comprehensive review of different automatic methods to determine the optimum value for the spatial damping factor λ. For field data sets where
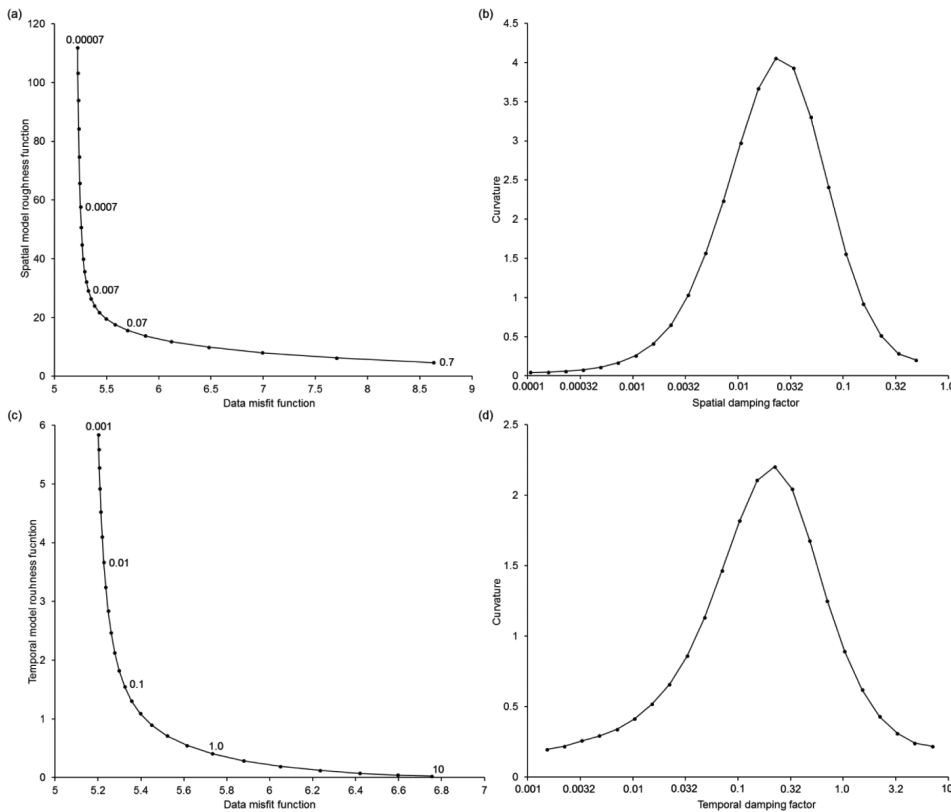
FIGURE 4

Example plots of L-curves to determine the optimum spatial and temporal damping factors. (a) Variation of spatial model roughness with data misfit for a range of spatial damping factor values (a few values are shown near the corresponding points), (b) variation of the curvature of the spatial L-curve with the spatial damping factor, (c) variation of temporal model roughness with data misfit for a range of temporal damping factor values, (d) variation of the curvature of the temporal L-curve with the temporal damping factor.

the noise level is not known, the L-curve method (Hansen 1998; Li and Oldenburg 1999; Gunther *et al.* 2006) may be used. The L-curve method basically examines the change in the data misfit with the damping factor. The use of this method for the time-lapse least-squares equation (2) has an additional complication in that there are two damping factors: λ for the spatial roughness filter and α for the temporal roughness filter. We thus use a two-step approach. In each iteration we first use the L-curve method to estimate the optimum value for the spatial roughness filter damping factor λ, as it generally has a larger effect on the data misfit, all the while keeping the temporal roughness filter fixed. Next λ is kept fixed and the L-curve method is applied in a similar way to estimate the optimum value for α. Figure 4(a) shows an example of the spatial model roughness $M(\lambda)$ versus the data misfit $D(\lambda)$ curve for a 3D data set (for the synthetic model described in the next section), while Fig. 4(b) shows the corresponding curvature versus the damping factor plot. The equations for the data misfit and model roughness functions for the L2-norm method (Farquharson and Oldenburg 2004) are as follows:

$$D(\lambda) = \sum_{i=1}^{i=mt} \left(d_o(i) - d_{cL}(i) \right)^2 \tag{3}$$

$$M(\lambda) = \left\| \mathbf{W} \mathbf{r}_L \right\|^2 \tag{4}$$

where d_o and d_{cL} are the logarithms of measured and calculated apparent resistivity values. The calculated apparent resistivity values for the different trial models, within the L-curve algorithm, are estimated using a linear approximation (Farquharson and Oldenburg 2004).

$$\mathbf{d}_{cL} \approx \mathbf{d}_c + \mathbf{J}^T \Delta \mathbf{r}_L \tag{5}$$

In this example, a trial value of about 0.1–0.2 is initially chosen for λ for the first iteration and equation (2) is solved for 25 damping factor values ranging from 0.01–100 times the trial value spaced logarithmically with six values per decade. The procedure is necessary to determine the corresponding changes in the model roughness $M(\lambda)$ and data misfit $D(\lambda)$ functions. The optimum damping factor value should be covered by such a large range. If the L1-norm method is chosen, the sum of the absolute value of the differences is used. One item of note is the data misfit and model roughness functions are dimensionless quantities as they are calculated from the difference in the logarithms of the resistivity values.

When the L-curve method is used for the temporal damping factor, the temporal model roughness is given by:

$$M_T(\alpha) = \left\| \mathbf{M} \mathbf{r}_L \right\|^2 \tag{6}$$

We use an initial value of 0.2 for α that is then refined by the L-curve method in each iteration. The sum of the squares of the difference in the logarithms of the resistivities of the corresponding model cells in adjacent time-lapse models is used.

As examples of typical temporal L-curves, Fig. 4(c,d) shows the temporal model roughness versus data misfit and curvature versus damping curves for the same data set. Note that the variation of the data misfit with the spatial damping factor λ (Fig. 4a) is greater compared to the temporal damping factor α (Fig. 4c). The curvature curve for the spatial and temporal damping factors shows a distinct maximum corresponding to the optimum damping factor. When using the L-curve method as described above, the optimum spatial and temporal damping factors usually converge to near constant values after a few iterations (Farquharson and Oldenburg 2004).

RESULTS
Synthetic model test
A set of temporally changing targets within a model 16 x 12 m are shown in Fig. 5. The initial model (Fig. 5a), considered as a baseline for comparison later, has a single high-resistivity block of 200 Ωm in the top layer within a homogeneous medium of 100 Ωm. In the second snapshot (Fig. 5b), a moderately high-resistivity block of 150 Ωm is added in the second layer and a low-resistivity block of 75 Ωm in the third layer. The sizes of the deeper blocks are increased in the third snapshot (Fig. 5c). All the possible dipole-dipole measurements in both the x- and y-directions with a geometric factor of less than 1056 m (which corresponds to a dipole-dipole array with a dipole spacing $a = 1$ m and maximum dipole separation $n = 6$) are used as the synthetic test data set. The measurements are made along 12 lines in the x-direction and 16 lines in the y-direction. The spacing between the adjacent electrodes along each line, as well as the spacing between the lines, is 1 m. As such, a total of 2604 data points were generated for the test. Voltage-dependent random noise (Zhou and Dahlin 2003) was also added to the apparent resistivity values. The maximum amplitude of the noise for the data point with the lowest potential value was set at 15%. This is equal to 1.9 mV for this particular data set if the current is 1 A. When converted to apparent resistivity values, the noise level is smaller when the geometric factor is smaller. The largest geometric factor is about 56 times larger than the smallest geometric factor but the average noise level for the apparent resistivity values of the entire data set is only about 1.1%.

We used the L1-norm for both the data misfit and spatial model roughness (Loke *et al.* 2003) in the inversion of the data set based on the blocky nature of the targets. The use of the L1-norm method for the data misfit makes the inversion procedure less sensitive to noise (Farquharson and Oldenburg 1998). For this data set, the L-curve method selected a value of about 0.02 for the spatial damping factor and values of 0.07 and 0.72 respectively for the L1-norm and L2-norm temporal damping factors at the final iteration.

Initially, inversions of the three snapshots were carried out independently with no temporal constraints. Figure 6(a–c) shows the inversion model sections for the three snapshots. The average data misfit is 1.2%, which is slightly higher than the noise added.

The three blocks are fairly well resolved, with both target foot-print and target values represented well in the inverse model results. Note, however, that the deepest layer shows the most significant distortions in the modelled resistivity due to the added noise. This is because the apparent resistivity values for the arrays with the largest spacings at $n = 6$ (i.e., those measurements with the deepest depth of investigation) also have the highest relative noise levels due to the larger geometric factors.

The inversion models for the three snapshots obtained using the L2- and L1-norm (Kim *et al.* 2010) temporal constraints are shown in Fig. 6(d–i). The inversion models obtained using the temporal constraints show more uniform resistivity values in the last layer close to the true value of 100 Ωm compared to the models obtained without the temporal constraint. The use of a temporal constraint has significantly reduced the distortions due to the added noise by reducing the variability across time.

The differences in the quality of the models by the three inversion methods are more clearly shown by plots of the chang-es in the resistivity of the second and third snapshots compared to the first model using the different temporal constraints (Fig. 7). In Fig. 7(a) and Fig. 7(e), higher distortions in the last two layers of the inversion model with no temporal constraints are visibly demonstrated. Differences of more than 20% in the model resistivity from the true value are observed. In compari-son, the difference sections for the L2-norm (Fig. 7b and Fig. 7f)

and the L1-norm (Fig. 7c and Fig. 7g) temporal constraints show relatively uniform values with maximum deviations of about 5% and 0.3%, respectively.

The second snapshot with no temporal constraints shows average changes of +39% and –20% at the locations of the two blocks (Fig. 7a), while the third time-series model (Fig. 7e) shows changes of +38% and –20%. These are in reasonable agreement with actual changes in the synthetic model of +50% and 25% (Fig. 7d). The average changes observed for the snap-shots with the L2-norm temporal constraint are +23% and –13% for the second temporal model (Fig. 7b) and +26% and –15% for the third temporal model (Fig. 7e). The smaller changes obtained with the L2-norm models are probably due to the temporal smoothness constraint that is added in addition to the spatial smoothness constraint. The use of the L2-norm tem-poral constraint tends to cause the anomaly to be more spread out where a sharp boundary becomes a smooth boundary. The differences between sharp and smooth boundaries are more clearly illustrated in the depth profile plots shown in Fig. 8. Figure 8(a,b) shows the change in the resistivity from the sec-ond and third snapshots for a model cell located at (3.5, 6.5), which is close to the centre of the higher resistivity block in the second model layer. The true model has a 50% increase in the resistivity in the second layer only. The corresponding anomaly in the L2-norm model has a lower maximum amplitude and is
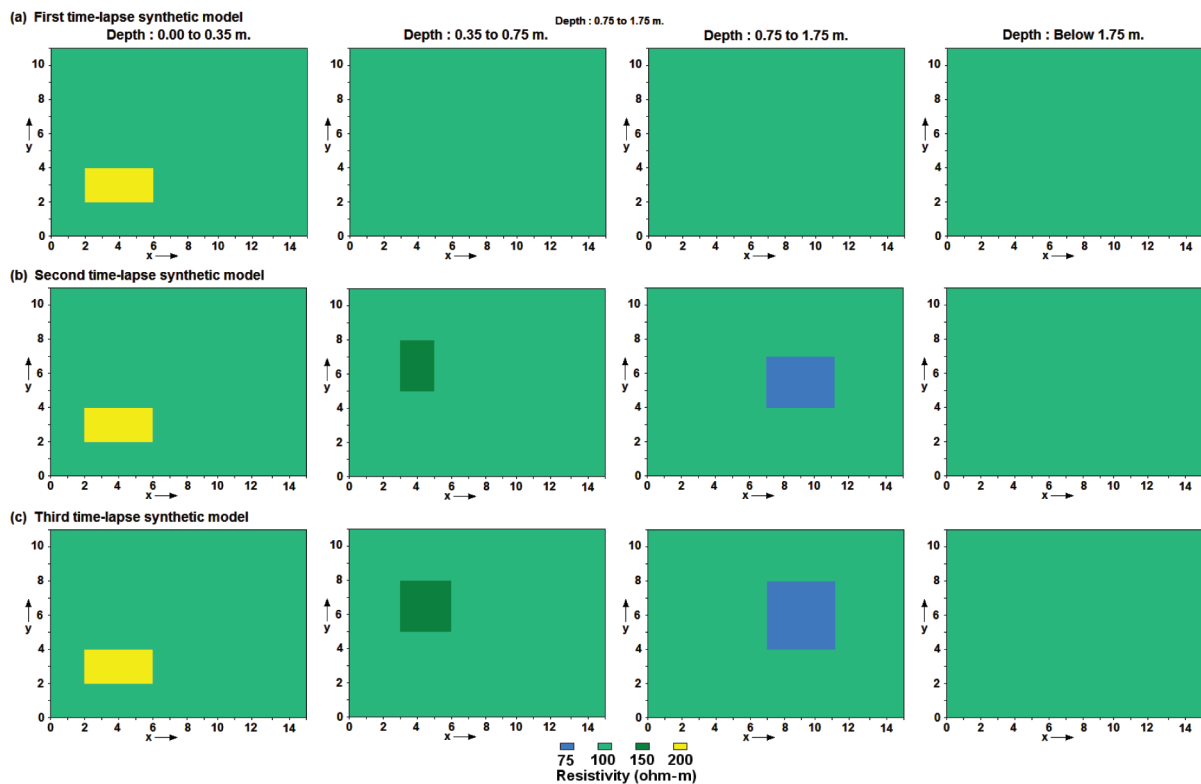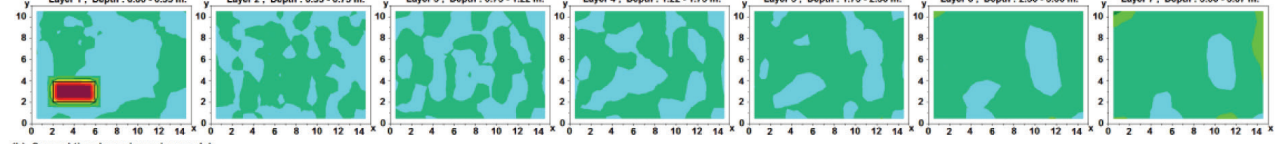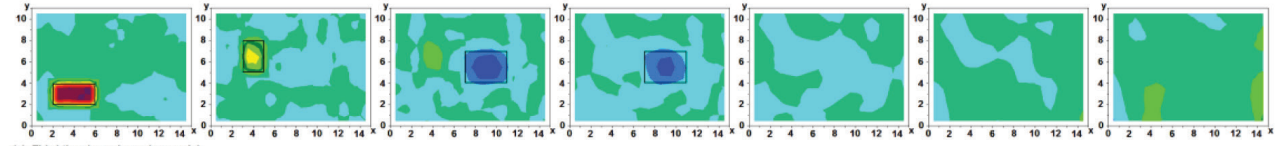

FIGURE 5
Three time-lapse test models used to generate the synthetic data set.
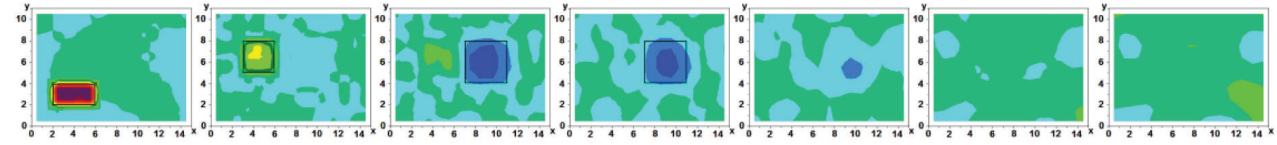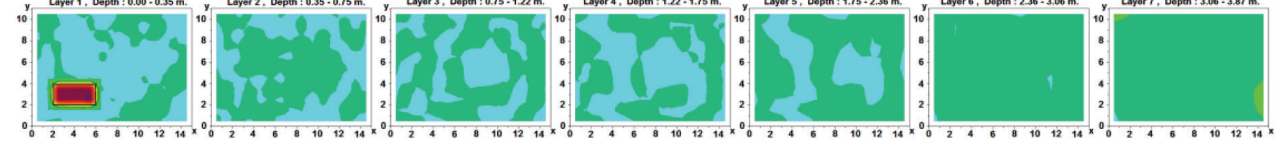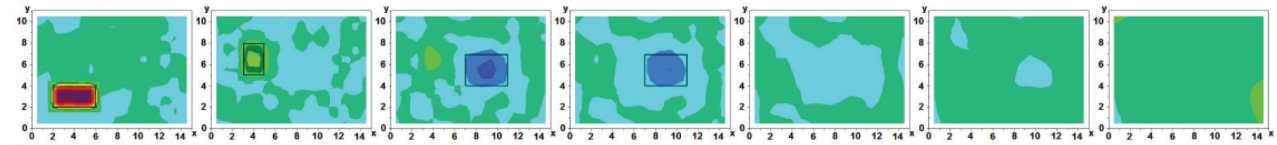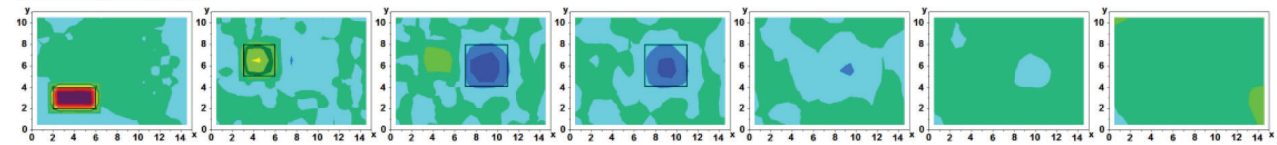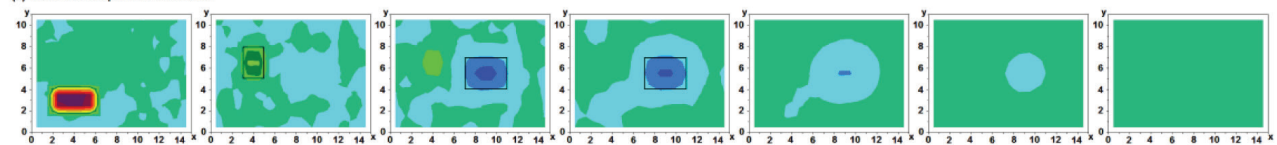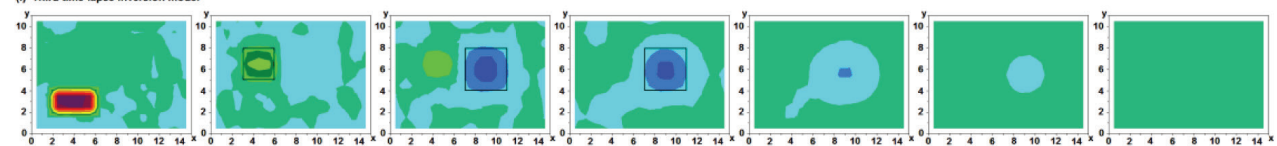
FIGURE 6

Inversion results using no time-lapse constraint showing the (a) first, (b) second and (c) third time-lapse models. The outlines of the true boundaries of the blocks are also shown for comparison. Each row shows an x-y cross-section of a model layer starting from the top layer on the left to the deepest layer on the right. Similar inversion results using a L2-norm time-lapse constraint are shown in (d), (e) and (f). The inversion results using a L1-norm time-lapse constraint are shown in (g), (h) and (i).

FIGURE 7

The change is the model resistivity of the second time-lapse model compared to the first model using (a) no time-lapse constraints, (b) a L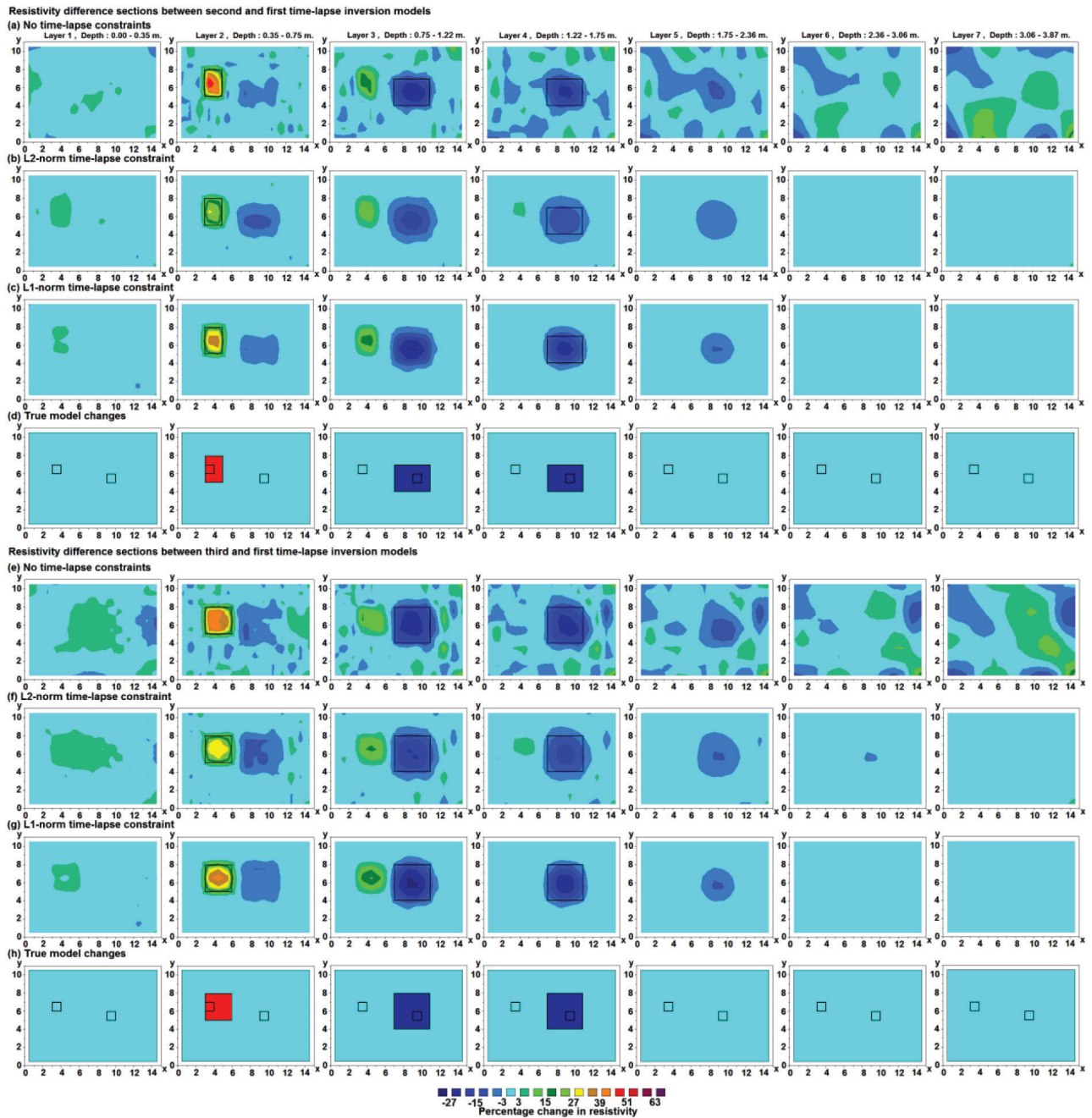2-norm time-lapse constraint, (c) L1-norm time-lapse constraint and (d) the true model changes. Similar model difference sections between the third and first time-lapse models are shown in (e), (f), (g) and (h). The small black rectangles in (d) and (h) show the location of the cells used in the depth profile plots in Fig. 8.

more spread out (extending to the fourth layer) compared to the models with no time-lapse and L1-norm time-lapse constraints. A similar pattern is shown by the depth profile plot for a model cell located at (9.5, 5.5) near the centre of the low- resistivity anomaly. The corresponding anomaly in the L2-norm model extends up to two layers below the true bottom boundary. This is similar to the effect of using the L2-norm spatial model con-

straint (Loke *et al.* 2003). The profile plots also show that the independent inversions model is more greatly affected by noise in the deeper layers.

The average changes at the two blocks observed for the inversion models with the L1-norm temporal constraint are +32% and –19% for the second temporal model (Fig. 7b) and +32% and –19% for the third temporal model (Fig. 7e). The

amplitudes of the changes are slightly lower than the models without time-lapse constraints but significantly higher than the L2-norm model.

To quantitatively demonstrate the differences in the accuracy of the models, we also calculate the model misfits between the true (r_t) and calculated (r_c) model values using:

$$\delta_m = \sum_{i=1}^{n} \left[\log(r_t(i)) - \log(r_c(i)) \right]^2 \tag{7}$$

Table 1 shows the model misfits for the different snapshots and time-lapse inversion constraints. For all models, the misfit for the independent inversion model is significantly higher compared to the L2-norm method, which is in turn higher than the misfit for the L1-norm method. The sum of the misfits for all the three snapshots for the independent inversions method is about 20% higher than the L2-norm method, while the L1-norm model misfit is about 23% lower than the L2-norm method. The use of a time-lapse constraint significantly increases the accuracy of the inversion models, probably by reducing the distortions from the added noise. The L1-norm method performs better than the L2-norm method as the constraints correspond more closely to the abrupt nature of the temporal changes.

The time-lapse method should also accurately estimate temporal changes in the resistivity. We thus also calculate the relative change in the resistivity for all the model cells. As an example, the relative change in the resistivity between the second (r_2) and first snapshot (r_1) is calculated using:

$$\partial_{21}(i) = \left[r_2(i) - r_1(i) \right] / r_1(i) \tag{8}$$

The relative changes obtained from the time-lapse models are then compared with the true relative changes (Fig. 7e and Fig. 7h). Table 2 gives the sum of the squares of the differences between the true relative change and those obtained by the dif-

TABLE 1

Model misfits for the inversion models obtained using the different time-lapse constraints.

	Independent	L2-norm	L1-norm
Model 1 misfit	0.232	0.162	0.084
Model 2 misfit	0.336	0.278	0.227
Model 3 misfit	0.374	0.327	0.280
Sum of model misfits	0.942	0.767	0.591

FIGURE 8

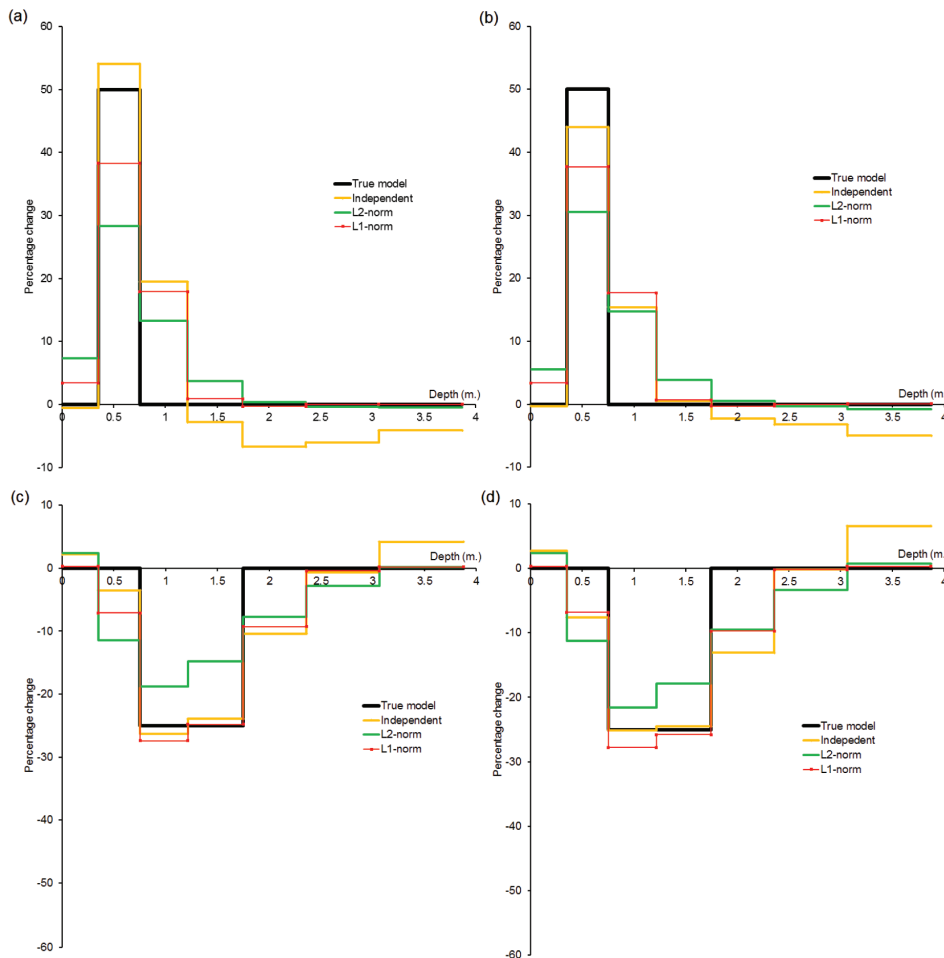Plots of the percentage change in the resistivity versus depth. (a) and (b) are for a model cell with a centre at (3.5, 6.5). (a) The change between snapshots 2 and 1, (b) the change between snapshots 3 and 1. (c) and (d) are similar plots for a model cell with a centre at (9.5, 5.5). Note the L2-norm time-lapse model (green line) shows a broader anomaly compared to the other inversion methods.

TABLE 2
Relative model change misfits for the inversion models obtained using the different time-lapse constraints.

	Independent	L2-norm	L1-norm
Model 2 change	2.090	1.284	0.647
Model 3 change	2.753	1.647	0.946
Sum of model misfits	4.843	2.931	1.593

ferent inversion methods for all the model cells. A similar result is obtained in that the L1-norm method gives the smallest misfits, followed by the L2-norm and independent inversion methods.

Field surveys

We now present the results from two field surveys. The L1-norm constraint is used for the data misfit and also the spatial model roughness for both data sets. For the first data set, we also show the difference sections obtained using independent inversions and the L1-norm and L2-norm time-lapse constraints, as an example of the use of the different methods for a field survey 3D data set.

Filborna landfill monitoring survey, Sweden

A resistivity survey was carried out to map the variation in fluid and gas content in a landfill site at Helsingborg, Sweden where methane gas accumulation is of prime interest (Rosqvist *et al.* 2010). The predominant material in the investigated volume is mixed waste, with a layer of cover material on top. According to the waste company the cover material (starting from the surface) consists of 0.4 m compost, 0.8 m excavation masses, 0.3 m gravel and 0.3 m clay, plus possibly 0.1–0.2 m compost (giving a maximum thickness of about 2 m for the cover material), under which there is waste. However the thickness of the cover material is a high variable and at some places intermittent, across the landfill site. The groundwater level is expected at some metres depth according to observations in the surrounding areas. The waste is underlain by sedimentary rock dominated by sandstone at depths beyond the depth penetration of the investigation presented here.

The survey data set consisted in 12 parallel 2D survey lines acquired with a pole-dipole array. Each line was composed of 21 electrodes with an electrodes spacing of 2 m along each line. The spacing between the lines was also 2 m. Eight sets of measurements were made at 3 hours apart for each day. It took nearly 3 hours to make each set of measurements with an ABEM Terrameter LS 12-channel resistivity meter. The data acquisition was done measuring induced polarization (IP) as well as resistivity using a duty cycle with 1 second current-on and current-off, where the timing is a compromise between acquisition speed and ability to capture the IP characteristics. Only the resistivity data results are presented here. It can be noted that even if only resistivity data were measured, shorter measurement cycle times lead to underestimation of the measured resistivity due to the large IP-effects associated with waste. Further details on the survey

procedure and geology of the survey area can be found in Dahlin *et al.* (2011).

The inversion model used cells of 1 m width so that large near-surface resistivity variations could be more accurately modelled. Higher damping factors were also used for the first two layers as well as diagonal roughness filters to reduce banding effects in the inversion model (Loke and Dahlin 2010). Initially an inversion was carried out for 12 daily data sets measured on 30th June–11th July 2011 at the same time of day (about 9 am). It was found that there was little change in the resistivity except between 2nd–4th July. The meteorological records indicated that there was heavy rainfall on 2nd July. Another inversion was then carried out using 26 data sets measured at every 3 hours from 6 pm on 1st July to 9 pm on 4th July in order to map these temporal changes more accurately. Each snapshot has 4176 data points. Out of the total of 108 576 data points for the 26 snapshots, there were 13 missing data points due to poor electrode contact caused by animal disturbances. From our experience with long-term monitoring systems, missing data points are fairly common. One advantage of the simultaneous 4D inversion method is that it does not require every snapshot to have the same number of data points, compared to the difference method that directly uses the apparent resistivity difference between snapshots (Labreque and Yang 2001).

The initial time-lapse resistivity model is shown in Fig. 9 as horizontal and vertical cross-sections. In parts of the model, as shown in the topmost horizontal section in Fig. 9(a), there is a distinct top layer with resistivity values mainly in the range of 20–57 Ωm. There is, however, a prominent high-resistivity linear band (resistivity values above 57 Ωm as indicated by yellow in the contour plot) running from the left to right of the topmost layer (Fig. 9a). This layer has a thickness of 0.8 m. The high-resistivity zone may consist of soil material with less clay content, or the clay layer is missing that leads to less water retention. Alternatively, the cover layer is very thin. In any case this zone is most likely to be more permeable than the surrounding soils with lower resistivity. More permeable areas tend to be more active in terms of biogenic gas movement, where increase in methane concentration is expected to lead to higher resistivity values as the water saturation decreases. Just below this higher resistivity band is a corresponding band of lower resistivity values (with values of less than 40 Ωm in some places) in layers 3–5 with a depth range of about 1.6–4.6 m (Fig. 9a).

The vertical sections (Fig. 9b) show the different layers more clearly. The top layer with resistivity values of generally below 57 Ωm and a thickness of between 0.5–1.5 m corresponds to the soil cover. Below the top layer is a high-resistivity layer with values between 57–400 Ωm representing the landfill waste material above the water table. The water table is, according to the model, located at a depth of about 5 m indicated by a sharp decrease in the resistivity values to below 10 Ωm towards the bottom of the model, in good agreement with the background information.
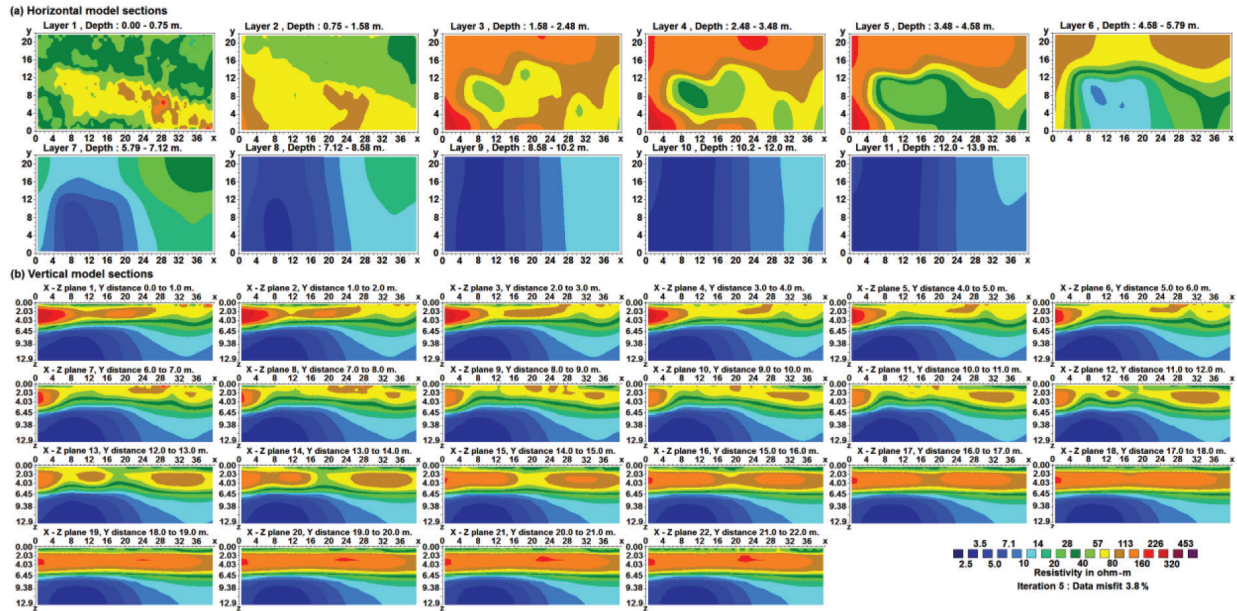
FIGURE 9

Inversion model for the Filborna monitoring survey shown in the form of (a) horizontal and (b) vertical cross-sections.
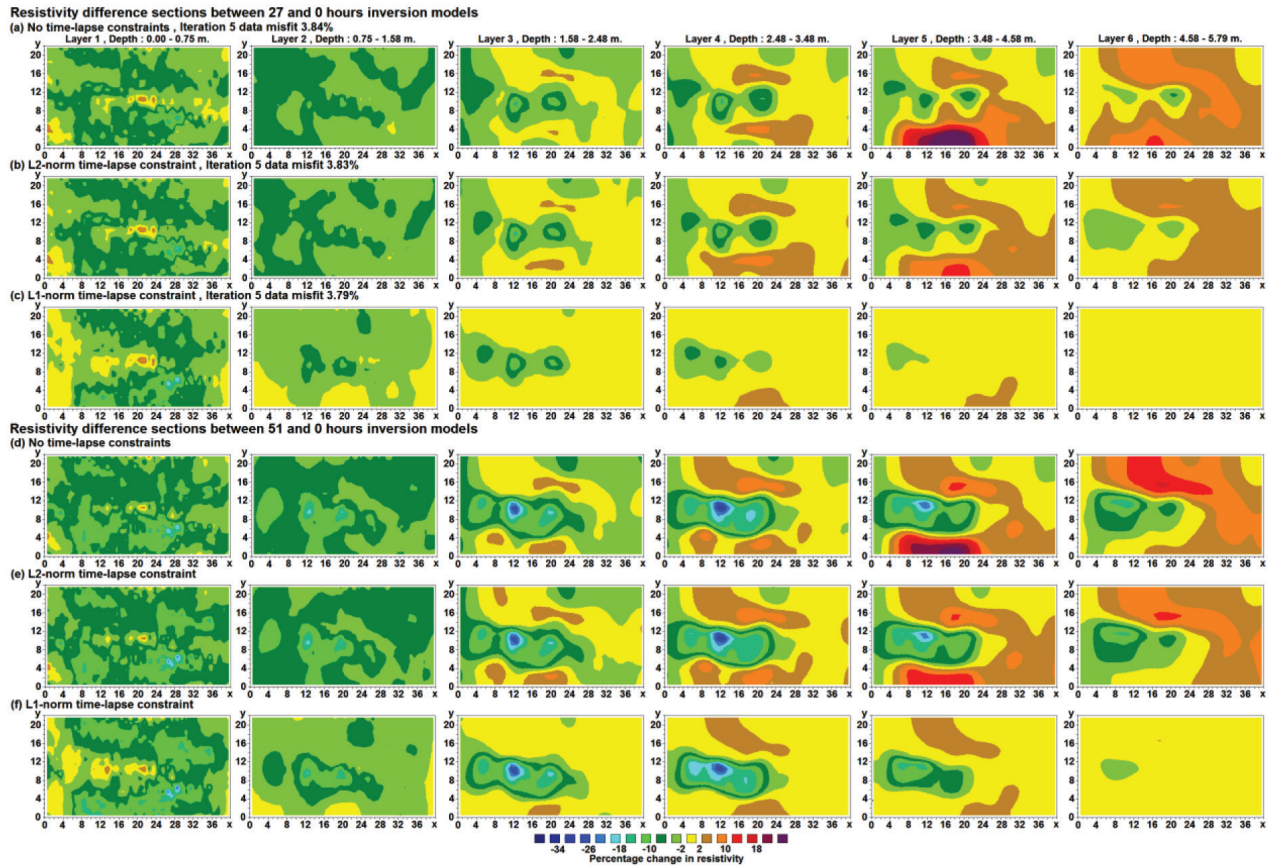

FIGURE 10

The change is the model resistivity of the 27 hours time-lapse model compared to the first model using (a) no time-lapse constraints, (b) a L2-norm time-lapse constraint and (c) a L1-norm time-lapse constraint. Similar model difference sections between the 51 hours and first time-lapse models are shown in (d), (e) and (f).
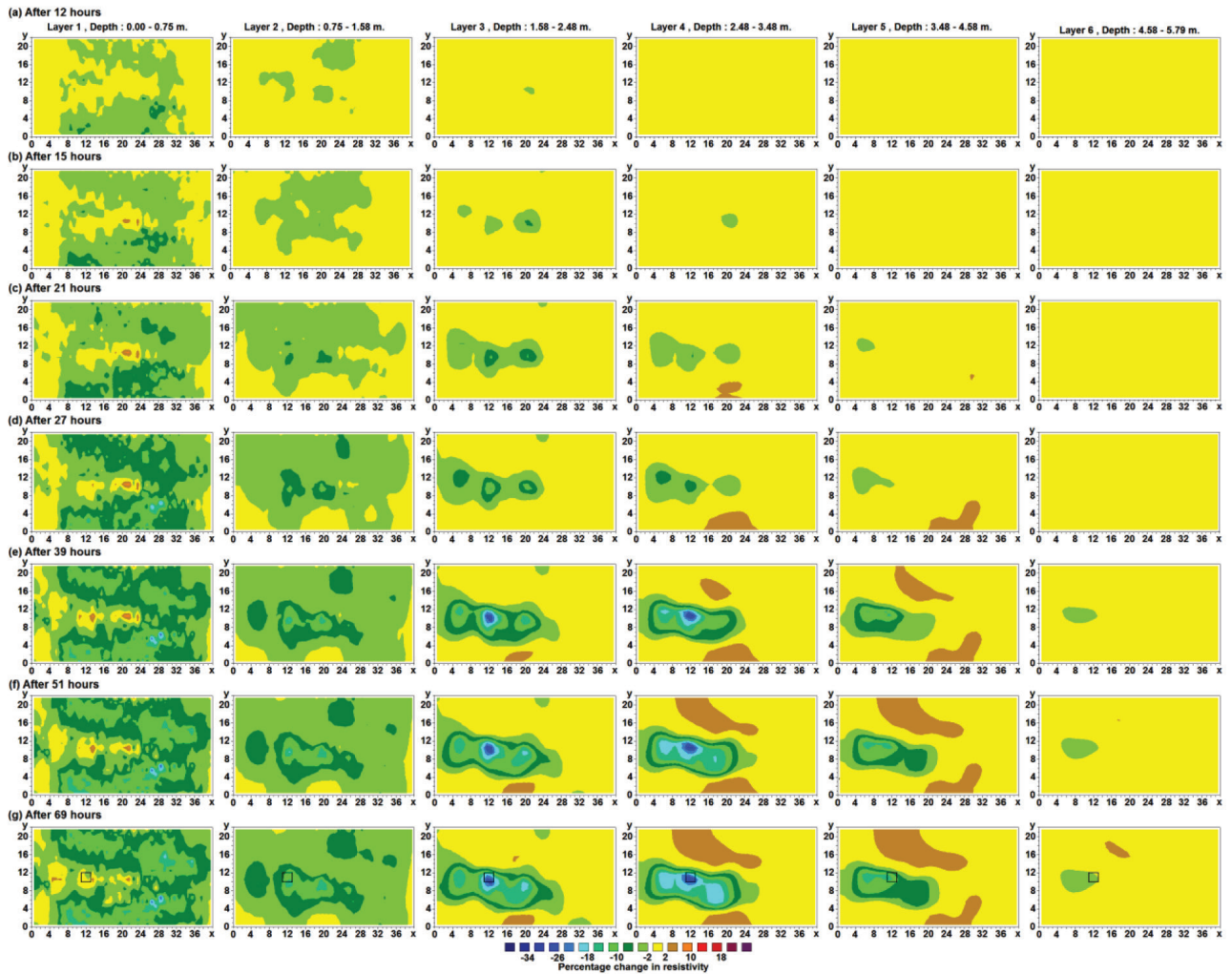
FIGURE 11

Resistivity difference sections for models at (a) 12 hours, (b) 15 hours, (c) 21 hours, (d) 27 hours, (e) 39 hours, (f) 51 hours and (g) 69 hours from the initial data set. The small black rectangle in the last row shows the location of the cells used in the time-profile plots in Fig. 13.

We carried out inversions of the time-lapse data set using independent inversions and the L1-norm and L2-norm time-lapse constraints. The inversion models show that the maximum change in the resistivity occurred after about 51 hours from the initial data set. As an example of the results obtained with the different methods, Fig. 10 shows the difference sections for the models at 27 and 51 hours. In Fig. 10(a), the fifth layer in the difference section for the independent inversions model (at 27 hours) shows a prominent increase in the resistivity of up to about 29% at the region bounded by the y-coordinate between 0–4 m and the x-coordinate between 8–24 m. The resistivity is generally expected to decrease with time due to rainfall during the survey period. The increase in the resistivity is most likely to be an artefact (possibly due to noise) as the model resolution decreases with depth as well as towards the sides where there is less data coverage. The independent inversions method attempts to minimize the data misfit for each snapshot individually (sub-

ject to the spatial smoothness constraints) without taking into consideration the results of the other snapshots. This artefact is greatly reduced to less than 12% when a L2-norm time-lapse constraint is used (Fig. 10b) and almost completely eliminated with a L1-norm time-lapse constraint (Fig. 10c). Note there are also significant increases in the sixth layer for the model with independent inversion (Fig. 10a) that are likely artefacts due to noise. The artefacts are greatly reduced with a L2-norm temporal constraint (Fig. 10b) and essentially eliminated with a L1-norm temporal constraint (Fig. 10c).

A similar effect is seen in the difference sections for the model at 51 hours (Fig. 10c–e). The difference sections for the 51 hours model using independent inversions show a prominent artefact at the region bounded by the y-coordinate between 14–24 m and the x-coordinate between 12–28 m in the fifth and sixth layers; a resistivity increase of up to 16% is observed here (Fig. 10d). The same anomaly is significantly reduced when a L2-norm time-

lapse constraint is used (Fig. 10e) and almost eliminated with a L1-norm time-lapse constraint (Fig. 10f). All the difference sections for the 51 hours model show a prominent decrease in the resistivity in the third to fifth layers, between the y-coordinate of 6–14 m and between the x-coordinate of 2–22 m, which is likely to be a real anomaly. Note that the conductive anomaly in the fourth column in Fig. 10(e) for the L2-norm model is slightly more pronounced than in the corresponding section in the L1-norm model (Fig. 10f). This is probably partly caused by an

artefact in the L2-norm model associated with the large areas with resistivity increases of +2 to +10% on both sides of the conductive anomaly in the y-direction. It is well-known that in the space domain the L2-norm constraint tends to produce an oscillatory structure near a boundary with overshoots at the high-resistivity side and undershoots at the low-resistivity side of the boundary (Farquharson and Oldenburg 1998). A similar effect probably occurs in the temporal domain that makes the decrease in the resistivity values in the conductive zone more pronounced.
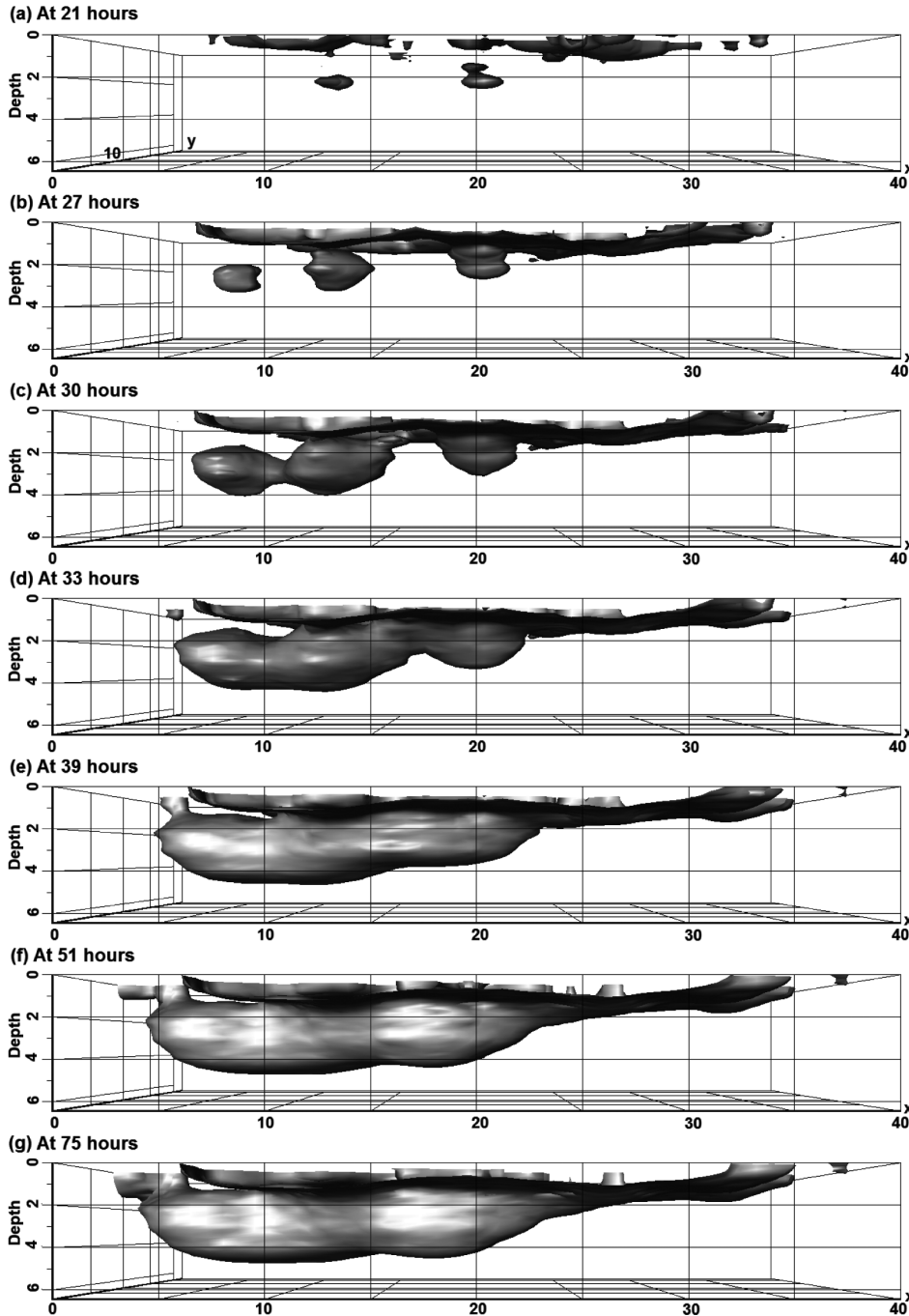

FIGURE 12
3D iso-surface plots showing the positions of the –6% resistivity change boundary with time.

Anomalies in the independent inversions difference sections, which are significantly reduced when a time-lapse constraint is used, could be artefacts, while those that are present regardless of the constraint used are likely to be real. The L1-norm time-lapse constraint appears to be more effective in suppressing the artefacts, which is similar to the results obtained previously with the synthetic model data set. The inversion of the same data set with different time-lapse constraints is useful in helping to separate real anomalies from artefacts.

Figure 11 shows a series of snapshots with the percentage change in the resistivity values for the models at 12–69 hours from the initial data set using the L1-norm time-lapse constraint. No significant change in the resistivity values (of more than 2%) was observed before 12 hours. At 12 hours, there is a slight decrease in the resistivity values in the top layer (green regions in Fig. 11a) that corresponds to the start of a high-precipitation event lasting for about 6 hours. The decrease in resistivity becomes more widespread at 15 hours where it now spreads to layer 2 (0.75–1.58 m depth) and slightly to the third layer (1.58–2.48 m). At 21 hours (Fig. 11c) the low-resistivity values spread downwards to layer 4 (2.48–3.48 m) and regions with changes of more than –6% are now more widespread in the top layer. At 39 hours (Fig. 11e) it spreads to layer 5 (3.48–4.58 m) while regions with changes of more than –30% are observed in layers 3 and 4. The process continues as shown by the sections at 51 hours (Fig. 11f) after which there are very small changes (Fig. 11g). No significant changes (more than 2%) were observed in layers deeper than the sixth (below 5.79 m depth) because they lie within the water table zone. The largest changes in layers 3–5 occur within a permeable zone that provides a path for the rainwater to migrate downwards. Outside of the permeable zone, there are no significant changes in the resistivity within the third and deeper layers. This is because the landfill material is less permeable, which confines the rainwater to the two top layers.

Figure 12 shows iso-surface plots of the –6% resistivity change boundary, which provides a set of 3D views of the movement of the rainwater. At 21 hours (Fig. 12a), or about 10 hours after the start of the downpour, most of the water is still confined to near the surface. At 27 hours (Fig. 12b) more water has migrated downwards, which then forms a significant plume at 30 hours (Fig. 12c), finally reaching to 4 m depth at 33 hours (Fig. 12d). At 39 hours (Fig. 12e) the bottom boundary of the plume has moved slightly below 4 m accompanied by a greater lateral migration. A slight increase in the volume of plume is observed at 51 hours (Fig. 12f), after which there were no significant changes up to 75 hours (Fig. 12g).

Figure 13 shows a plot of the average resistivity change calculated from four neighbouring model cells centred around an x-y location of (12.0, 11.0). We use the average resistivity change for a group of neighbouring cells to reduce the effect of spurious variations in any individual cell. The location includes the region with the largest decrease in the resistivity values in layer 4 and lies within the zone that is expected to be more permeable. A plot of the cumulative rainfall (as measured starting from 23rd June 2011) is also shown in the plot. There is slight rainfall starting at about 6 hours with the heaviest rainfall between 9–15 hours. A second minor rainfall event occurred between 27–28 hours. Correspondingly a slight decrease in the resistivity of the topmost layer is observed starting from about 9 hours. The resistivity variation in the topmost layer is slightly different from the deeper layers, which show an initial rapid
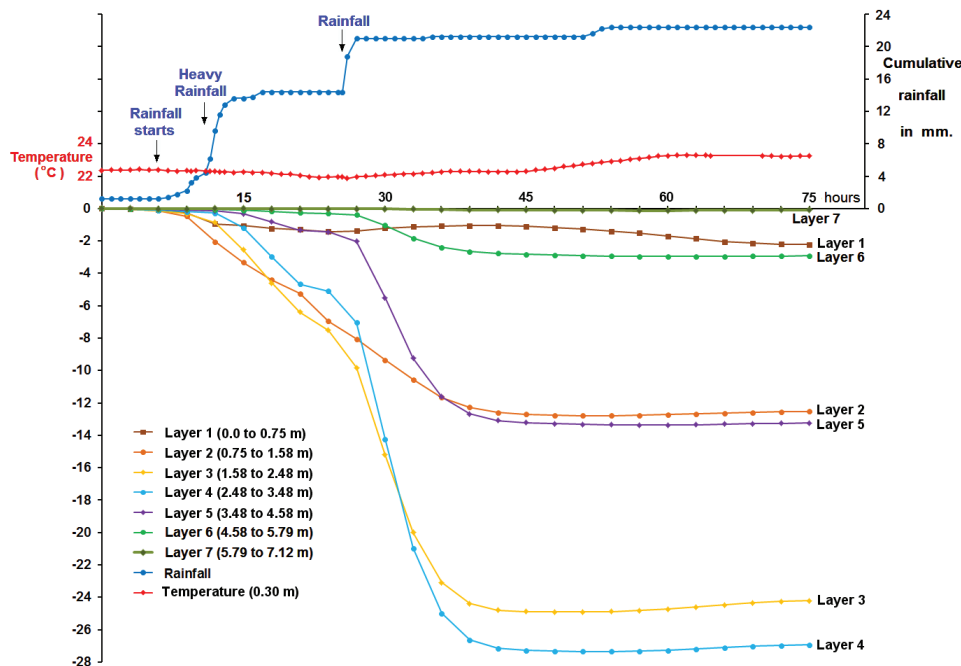

FIGURE 13

Average change in resistivity with time for four model cells centred around the (12.0, 11.0) location in the different layers. A plot of the cumulative rainfall and temperature (from a probe at 30 cm depth) is also shown.
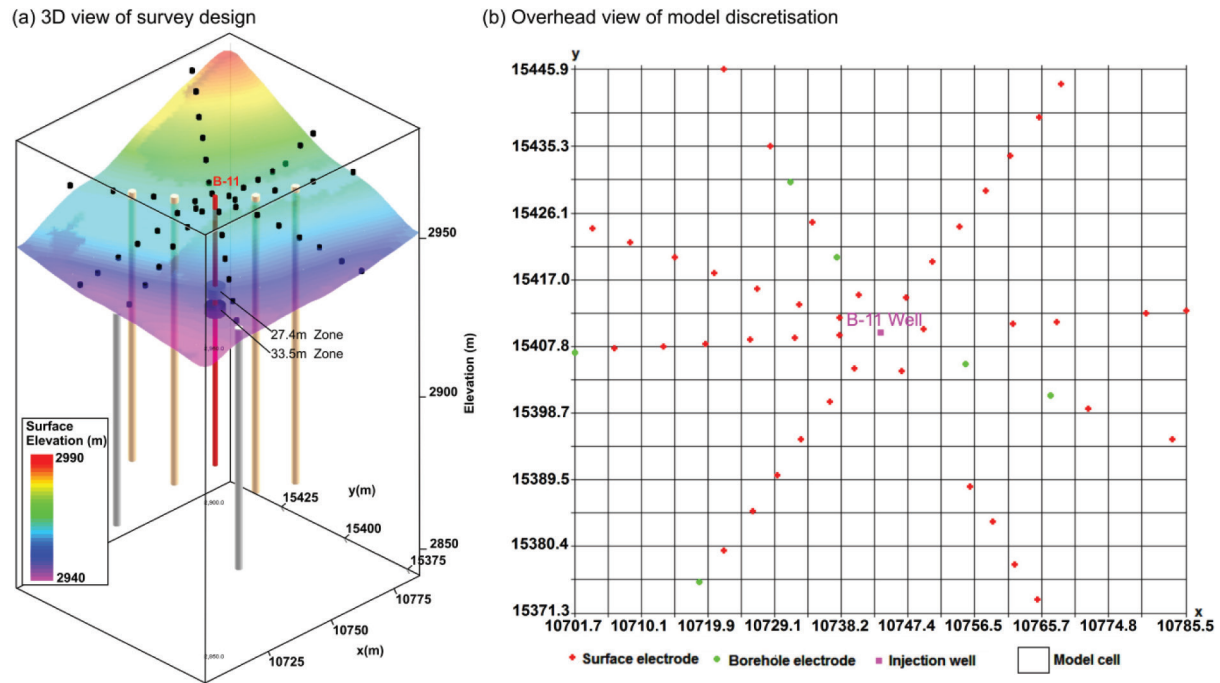
FIGURE 14

(a) Layout of the borehole injection survey with positions of the surface and borehole electrodes shown together with the topography. In the inversion model, the x and y axes correspond to the 'easting' and 'northing' directions. (b) Overhead view of the model discretization grid showing positions of the electrodes and injection well. The model grid has a spacing of 4.6 m in both the x- and y-directions, except near the ends where a spacing of 6.1 m was used to include the outermost electrodes.

decrease followed by almost constant values. The difference could be partly due to the combined effects of rainfall, temperature variations, moisture evaporation and migration of gas from the deeper layers on the resistivity values. The topmost layer also shows greater lateral variations in the resistivity and probably has larger variations in hydrological properties such as porosity and permeability. It has areas with high-resistivity values that could be composed of coarse material such as gravel or concrete. The air temperature varies from about 13–36°C during this period with a dominant diurnal variation. A temperature probe 5 cm below the surface shows a much smaller variation of 19–26°C, while another probe at 30 cm depth shows a very small variation of 22–24°C (Fig. 13).

The decrease in resistivity in layer 2 starts a few hours after the start of the rainfall event (Fig. 13). The drop in resistivity observed in layer 3 occurs well before a similar change in layer 4, which in turn occurs much earlier than layer 5. The largest average decrease in resistivity of nearly –28% occurs in layer 4. After about 51 hours the resistivity does not change significantly. There appears to be a slight increase in the resistivity after 51 hours in layers 3 and 4 of about 1% that could be due to the movement of water to the deeper layers after the rainfall had ceased. The amplitude of the resistivity changes in layers 5 and 6 are progressively smaller as they lie closer to the water table. The change in the resistivity is highly non-linear with most of the

changes occurring between the 12–36 hours marks. The change in the resistivity with time is clearly shown despite the possibility of smoothing of the temporal resistivity variations ('time smearing') due to changes during the time taken to carry out a single set of measurements.

Injection well experiment, USA

An experiment was conducted to test the feasibility of using a 3D ERT survey to map the movement of a solution (barren leachate comprising dilute sodium cyanide) injected at high pressures into an engineered rock pile (or heap). The injections were designed to increase the extraction of gold as a means of secondary recovery after surface leaching had ceased. The injections were carried out with an injection skid designed to push a solution at pressures that exceed the lithostatic overburden at rates in excess of 1000 gallons per minute.

The injection experiment and resistivity surveys were carried out at the Cripple Creek and Victor Gold Mine, in Colorado, USA from 20–28th September 2011. Resistivity measurements were acquired with the Geotection 180-channel resistivity monitoring system (Rucker *et al.* 2013). A total of 150 electrodes were incorporated into the domain for a complete 3D acquisition with a pole-pole array, including 48 surface electrodes placed along eight radials, 94 electrodes within six boreholes and eight long electrodes taken from the series of steel-cased injection wells installed
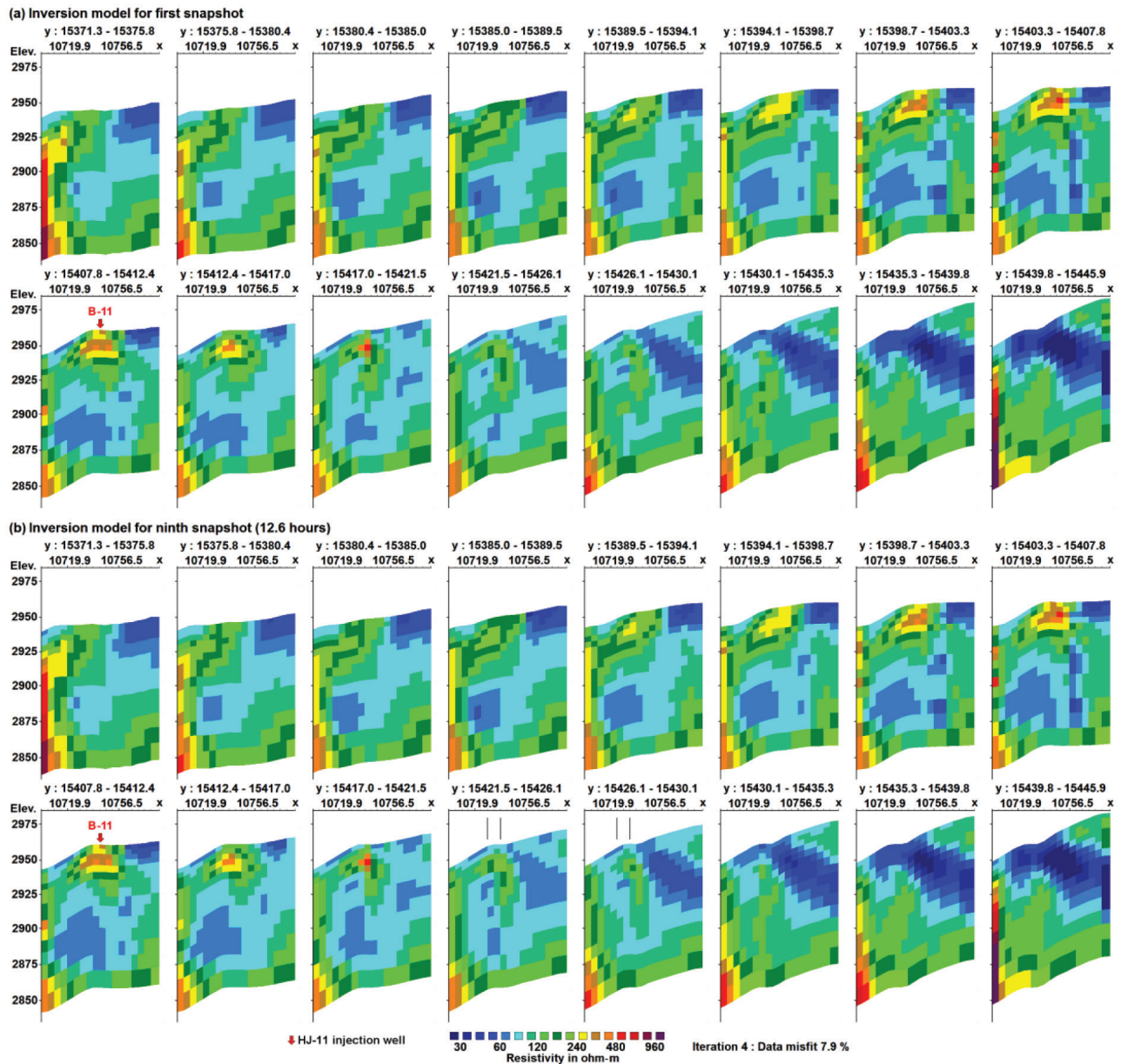
(a) Inversion model for first snapshot

(b) Inversion model for ninth snapshot (12.6 hours)

FIGURE 15

(a) Vertical cross-sections for the initial time inversion model. The cross-sections are in the x-z plane. (b) Similar cross-sections for the ninth inversion model for data taken at 12.6 hours later. The vertical black lines in the last row in (b) mark the positions of the model cells used in the time-profile plots in Fig. 17.

within the heap. Each snapshot took approximately 14 minutes to complete, with each snapshot comprising a full reciprocal data set. Over the course of the campaign, 780 snapshots were acquired. Editing of the data included (1) removing electrodes that were performing poorly, (2) data rejection based on random noise and (3) comparing reciprocal errors (Rucker *et al.* 2013). After editing, 125 electrodes remained in the final data set.

A 3D view showing the surface topography and the positions of the electrodes on the surface and boreholes is provided in Fig. 14(a). The surface electrodes are arranged in a radial pattern

around the well that was used to inject the barren solution into the heap. The data coverage is very sparse towards the edges of the survey area due to the radial layout of the electrodes. An overhead view of the inversion model grid is shown in Fig. 14(b), where the model cells were square with 4.6 m sides. The model grid is independent of the layout of the electrodes so that it can accommodate a non-rectangular electrode arrangement. A finite-element mesh with 4 nodes per model cell in both the x- and y-directions was used (Rucker *et al.* 2010). The grid-independent method described by Spitzer *et al.* (1999) was used to calculate

the potentials at the electrodes positions. A distorted finite-element mesh is also used so that the surface elements of the mesh match the topography (Loke 2000).

A small sample of the injection results are presented in this paper, where 12 snapshots were extracted from the last day of monitoring, representing injections at depths of 33.5 m and 27.4 m below ground surface. For reference, collars are placed around the injection well at depths of 27.4 m and 33.5 m, representing injections at those depths in Fig. 14(a). The baseline from the survey was taken at 4:24 am and four snapshots were extracted during the 33.5 m injection (lasting approximately five hours), three snapshots for the 27.4 m injection (lasting 4 hours) and three snapshots extracted during the post injection draindown. Each snapshot has 6329 data points, averaged from the reciprocal data and the inversion model has 4320 cells. The inversion of the 12-snapshot data set took about 75 minutes for 4 iterations on a computer with a 3.2 GHz Intel 3930K hex-core CPU and 32 GB RAM using a 64-bit Windows 7 operating system. The time taken for the data processing is less than the survey time. This can be an important factor in surveys (such as extraction of natural resources, leakage from dams, landslide prone areas) where real-time monitoring is required. Lastly, only the model obtained with the L1-norm temporal constraint is presented for this field data set, as the previous examples show that this method is less sensitive to noise.

Figure 15(a) shows the spatial distribution of resistivity for the initial snapshot. The data are presented in the form of vertical slices in the x-z plane. The model shows the outlines of the hexahedral blocks as used in the model grid (instead of contoured sections) to illustrate the distorted finite-element mesh used to accommodate the topography. The location of the injection well (B-11) is also highlighted in the slice representing a y distance of 15 407.8–15 412.4 m. The results generally show low-resistivity regions due to the increased saturation from the previous seven days of injections. These injections occurred starting from the bottom of the well at a depth of 82.3 m, moving up 6.1 m for each subsequent injection zone. Typically, one or two zones would be occupied each day. The high-resistivity regions at the bottom-left corner of the sections (particularly the first two and last four sections) are probably artefacts due to the lack of data at the corners of the grid. Additionally, the low-resistivity banding in the north-east corner of the domain (shown in the upper-right hand corner of the first six sections) as well as the high-resistivity banding in the bottom-left corner of the last four sections in Fig. 15(a) may be questionable, again due to poor electrode coverage. Figure 15(b) shows the model for the ninth snapshot (9.8 hours after the injections commenced). Some changes are visible when compared with the model for the initial snapshot for the panels between y distances of 15 407.8 –15 435.3 m but it is difficult to trace the movement of the leachate from the resistivity sections alone.

Figure 16 shows the change in the resistivity in the form of 3D iso-contours that better illustrate the migration of the pregnant solution (dilute sodium cyanide solution laden with gold) through time. The iso-surface for the change of –4% in the resistivity was selected for this plot. The iso-surfaces are plotted at approximately 1.1, 2.4, 3.7 and 4.9 hours after the initiation of injection at the 33.5 m depth. Note the area with the largest change is located to the north of the well. This is probably due to differences in the subsurface permeability and structural non-uniformities within the heap created during end-dump construction (Rucker *et al.* 2009b). The heap has been built up over the past 20 years by trucks dumping fresh ore over the edge of older ore. Additionally, there were no significant artefacts (with changes of more than 4%) in these sections. This is because the time-lapse damping factor constrains the resistivity values to be similar in the different time models if changes are not supported by the data. Not unexpectedly, the volume through which the solution has diffused increases significantly with time. The flow of the solution was also monitored during the experiment by measuring the contact resistances at the subsurface electrodes (Rucker *et al.* 2013), which provides an independent means to
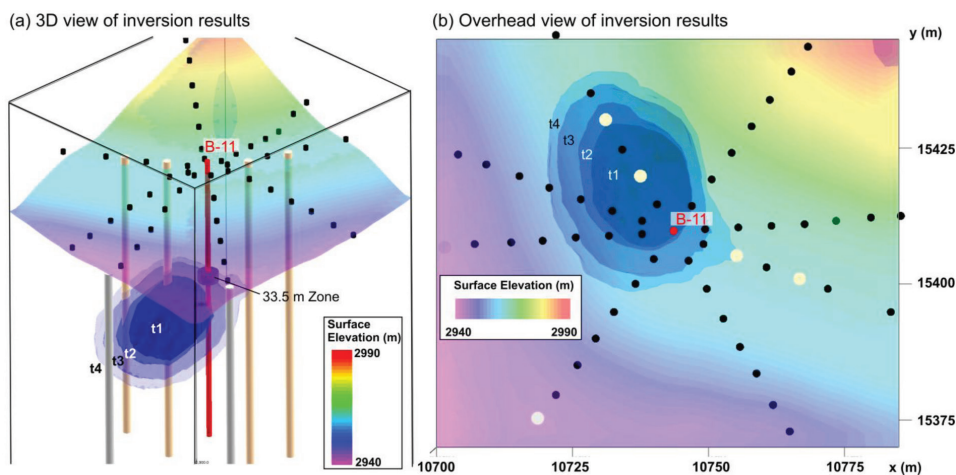

(a) 3D view of inversion results

(b) Overhead view of inversion results

FIGURE 16
Iso-surface contours for the –4% resistivity change at different times after the injection of the sodium cyanide solution (that started at 2.8 hours from the first data set in the snapshots used). *t*1 = 1.1 hours, *t*2 = 2.4 hours, *t*3= 3.7 hours, *t*4 = 4.9 hours.
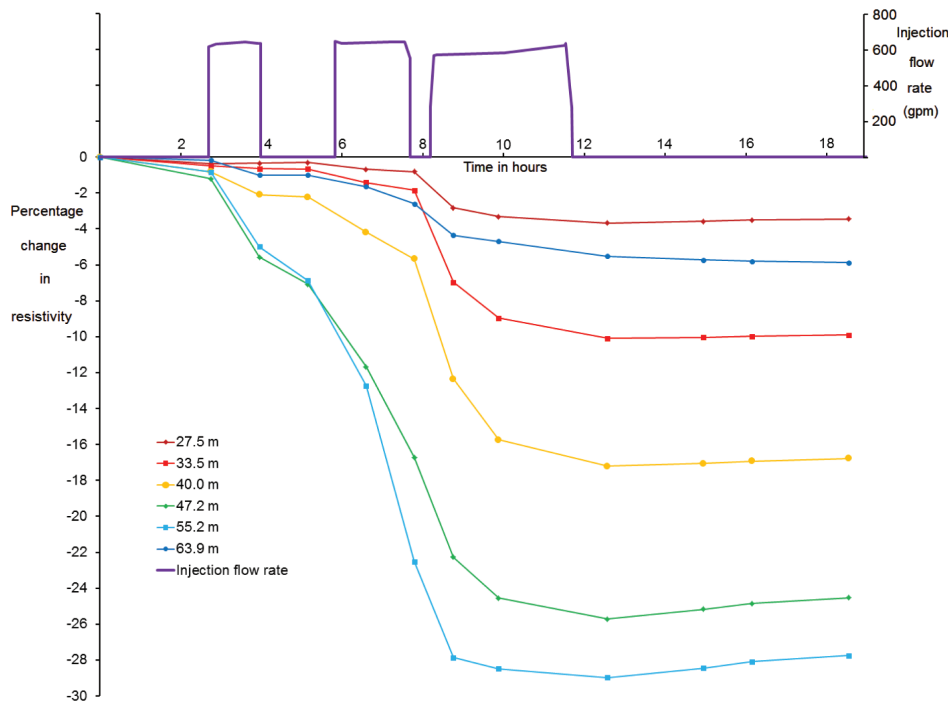
FIGURE 17

Average change of resistivity with time for four model cells centred around the x-y location of (10 733.7, 15 426.1) in the different model layers, together with a plot of the solution injection rate.

verify the development of the solution plume as shown by the resistivity images.

Figure 17 shows a plot of the average resistivity change calculated from four neighbouring model cells centred around an x-y location of (10 733.7, 15 426.1). The figure represents information from several depths, from 27.5– 63.9 m. The model cells at these locations show the largest change in the resistivity values, with the maximum at a depth of 55.2 m below the surface. The plot shows that the decrease in the resistivity reached an almost constant value after the cessation of injection at about 12 hours from the initial snapshot (Fig. 17). The resistivity increased slightly after injections stopped, which represents a draindown of the solution within the rock pile. Despite the challenging terrain and very sparse electrode layout, the survey has successfully mapped the solution migration with sufficient temporal and spatial detail to better understand and optimize the injection process.

CONCLUSION

The examples presented in this paper demonstrate that the constrained time-lapse method can successfully recover temporal changes in the resistivity even in the presence of noise for 3D resistivity surveys. In particular, the L-curve method, which is commonly used to determine the optimum spatial damping factor, can also be adapted to determine the appropriate value for temporal damping factors. The first example with the synthetic data set showed that the model obtained using independent inversions (without any temporal constraints) is the most sensitive to random noise. The artefacts are significantly reduced using a L2-norm temporal constraint and further reduced with a L1-norm

constraint. Furthermore, the L1-norm model gave the most accurate results in regards to position and reconstructed resistivity values, followed by the L2-norm model. Even for field data sets where the true structure is not accurately known, a comparison of the results obtained using independent inversions and the L2-norm and L1-norm temporal constraints is still useful in identifying likely artefacts. Anomalies that are common in models using the three different inversion methods are more likely to be real. In contrast, anomalies present in a model using independent inversions but that are significantly reduced with the L2-norm and L1-norm constraints, could be artefacts. This method to identify temporal changes that are likely to be real could be helpful in refining methods that use a spatially varying temporal damping factor (Karaoulis *et al.* 2011a; Kim and Cho 2011) to improve the resolution in selected regions.

From a field perspective, the inversion of a set of 26 time-series data sets from the Filborna landfill monitoring site successfully mapped the infiltration of rainwater down a permeable zone. The migration of a solution from an injection well was also successfully mapped using a combination of electrodes along six boreholes and eight radial lines on the surface, despite a difficult survey environment with significant topography.

Research is being carried out to include the exact time of each measurement in the inversion methodology (Kim *et al.* 2009) to reduce the effect of 'time smearing' when there is a significant change in the resistivity during the measurement of a single data set. The 'time smearing' effect may be less of a problem as the number of channels for acquisition hardware significantly increase, such as in the case of the injection well experiment presented here. The inversion method is also being extended for

the simultaneous inversion of 3D resistivity and IP time-lapse data using the complex resistivity (Kemna *et al.* 2000; Karaoulis *et al.* 2011b) method.

ACKNOWLEDGEMENTS

REFERENCES

Bentley L.R. and Gharibi M. 2004. Two- and three-dimensional electrical resistivity imaging at a heterogeneous remediation site. *Geophysics* **69**, 674–680.

Cassiani G., Bruno V., Villa A., Fusi N. and Binley A.M. 2006. A saline trace test monitored via time-lapse surface electrical resistivity tomography. *Journal of Applied Geophysics* **59**, 244–259.

Chambers J.C., Kuras O., Meldrum P.I., Ogilvy R.D. and Hollands J. 2006. Electrical resistivity tomography applied to geologic, hydrogeologic, and engineering investigations at a former waste disposal site. *Geophysics* **71**, B231–B239.

Dahlin T., Bernstone C. and Loke M.H. 2002. A 3D resistivity investigation of a contaminated site at Lernacken in Sweden. *Geophysics* **60**, 1682–1690.

Dahlin T., Rosqvist H., Johansson S., Månsson C.-H., Svensson M., Lindsjö M. and Loke M.H. 2011. Geoelectrical Monitoring for Mapping of Gas and Water Migration in Landfills. *Berichte Geologischen Bundesanstalt* **93**, 260-264. ISSN 1017-8880

Daily W., Ramirez A., Labrecque D. and Nitao J. 1992. Electrical-resistivity tomography of vadose water-movement. *Water Resources Research* **28**, 1429–1442.

Dey A. and Morrison H.F. 1979. Resistivity modeling for arbitrarily shaped three-dimensional shaped structures. *Geophysics* **44**, 753–780.

Farquharson C.G. 2008. Constructing piecewise-constant models in multidimensional minimum structure inversions. *Geophysics* **73**, K1–K9.

Farquharson C.G. and Oldenburg D.W. 1998. Nonlinear inversion using general measures of data misfit and model structure. *Geophysical Journal International* **134**, 213–227.

Farquharson C.G. and Oldenburg D.W. 2004. A comparison of automatic techniques for estimating the regularization parameter in nonlinear inverse problems. *Geophysical Journal International* **156**, 411–425.

Gharibi M. and Bentley L.R. 2005. Resolution of 3-D electrical resistivity images from inversions of 2-D orthogonal lines. *Journal of Environmental and Engineering Geophysics* **10**, 339–349.

Gunther T., Rucker C. and Spitzer K. 2006. Three-dimensional modelling and inversion of DC resistivity data incorporating topography – II. Inversion. *Geophysical Journal International* **166**, 506–517.

Hansen P.C. 1998. Rank deficient and discrete ill-posed problems. Society for Industrial and Applied Mathematics, PA.

Hayley K.L., Bentley L.R. and Gharibi M. 2009. Time-Lapse Electrical Monitoring of Salt-Affected Soil and Groundwater. *Water Resources Research* **45**, W07425.

Hayley K., Pidlisecky A. and Bentley L.R. 2011. Simultaneous time-lapse electrical resistivity inversion. *Journal of Applied Geophysics* **75**, 401–411.

Holcombe H.T. and Jiracek G.R. 1984. Three-dimensional terrain corrections in resistivity surveys. *Geophysics* **49**, 439–452.

Johansson B., Jones S., Dahlin T. and Flyhammar P. 2007. Comparisons of 2D- and 3D-inverted resistivity data as well as of resistivity- and IP-surveys on a landfill. Near Surface 2007, Istanbul, Turkey, Expanded Abstracts, P42

Karaoulis M.C., Kim J.-H. and Tsourlos P.I. 2011a. 4D active time constrained resistivity inversion. *Journal of Applied Geophysics* **73**, 25–34.

Karaoulis M., Revil A., Werkema D.D., Minsley B.J., Woodruff W.F. and Kemna A. 2011b. Time lapse three-dimensional inversion of complex conductivity data using an active time constrained (ATC) approach. *Geophysical Journal International* **187**, 237–251.

Kemna A., Binley A., Ramirez A. and Daily W. 2000. Complex resistivity tomography for environmental applications. *Chemical Engineering Journal* **77**, 11–18.

Kim K.-J. and Cho I.-K. 2011. Time-lapse inversion of 2D resistivity monitoring data with a spatially varying cross-model constraint. *Journal of Applied Geophysics* **74**, 114–122

Kim J.H., Yi M.J., Ahn H.Y. and Kim K.S. 2010. 4-D inversion of resistivity monitoring data using L1 norm minimization. Near Surface 2010, Zurich, Switzerland, Expanded Abstracts, A15

Kim J.H., Yi M.J., Park S.G. and Kim J.G. 2009. 4-D inversion of DC resistivity monitoring data acquired over a dynamically changing earth model. *Journal of Applied Geophysics* **68**, 522–532.

LaBrecque D.J. and Yang X. 2001. Difference inversion of ERT data: A fast inversion method for 3D in situ monitoring. *Journal of Environmental and Engineering Geophysics* **6**, 83–89.

Legault J.M., Carriere D. and Petrie L. 2008. Synthetic model testing and distributed acquisition DC resistivity results over an unconformity uranium target from the Athabasca Basin, northern Saskatchewan. *The Leading Edge* **27**(1), 46–51.

Li Y. and Oldenburg D.W. 1996. 3D inversion of magnetic data. *Geophysics* **61**, 394–408.

Li Y. and Oldenburg D. W. 1999. 3-D inversion of DC resistivity data using an L-curve criterion. Expanded Abstracts of the 69th Annual International Meeting of the Society of Exploration Geophysicists, 251–254.

Loke M.H. 2000. Topographic modelling in resistivity imaging inversion. 62nd EAGE Conference & Technical Exhibition, Extended Abstracts, D-2.

Loke M.H. 2011. Electrical resistivity surveys and data interpretation. In: *Solid Earth Geophysics Encyclopedia (2nd Edition) "Electrical & Electromagnetic",* (ed. H. Gupta), 276–283. Springer Verlag.

Loke M.H., Acworth I. and Dahlin T. 2003. A comparison of smooth and blocky inversion methods in 2D electrical imaging surveys. *Exploration Geophysics* **34**, 182–187.

Loke M.H. and Barker R.D. 1996. Practical techniques for 3D resistivity surveys and data inversion. *Geophysical Prospecting* **44**, 499–523.

Loke M.H., Chambers J.E. and Kuras O. 2011. Instrumentation, electrical resistivity. In: *Solid Earth Geophysics Encyclopedia (2nd Edition) "Electrical & Electromagnetic",* (ed. H. Gupta), 599–604. Springer-Verlag.

Loke M.H. and Dahlin T. 2010. Methods to reduce banding effects in 3-D resistivity inversion. Near Surface 2010, Zurich, Switzerland, Expanded Abstracts, A16.

Marescot L., Lopes S.P., Rigobert S. and Green A.G., 2008. Nonlinear inversion of geoelectric data acquired across 3-D objects using a finite-element approach. *Geophysics* **73**, F121–F133.

McGillivray P.R. and Oldenburg D.W. 1990. Methods for calculating Fréchet derivatives and sensitivities for the non-linear inverse problem: A comparative study. *Geophysical Prospecting* **38**, 499–524.

Oldenborger G.A, Knoll M.D., Routh P.S. and LaBrecque D.J. 2007. Time-lapse ERT monitoring of an injection/withdrawal experiment in a shallow unconfined aquifer. *Geophysics* **72**, F177–F187.

Rosqvist H., Leroux V., Dahlin T., Johansson S. and Svensson M. 2010. An evaluation of the potential of the geoelectrical resistivity method for mapping gas migration in landfills. *SAGEEP 2010 Proceedings (Volume 1)*, Keystone, Colorado, 369–378.

Rucker D.F., Crook N., Winterton J., McNeill M., Baldyga C.A., Noonan G. and Fink J.B. 2013. Real-Time Electrical Monitoring of Reagent Delivery during a Subsurface Amendment Experiment. *Near Surface Geophysics* **12**(1).

Rucker D.F., Fink J.B. and Loke M.H. 2011. Environmental monitoring of leaks using time lapsed long electrode electrical resistivity. *Journal of Applied Geophysics* **74**, 242–254.

Rucker D.F., Levitt M.T. and Greenwood W.J. 2009a. Three-dimensional electrical resistivity model of a nuclear waste disposal site. *Journal of Applied Geophysics* **69**, 150–164.

Rucker D.F., Loke M.H., Levitt M.T. and Noonan G.E. 2010. Electrical Resistivity Characterization of an Industrial Site using Long Electrodes. *Geophysics* **75**, WA95–WA104.

Rucker D.F., McNeill M., Schindler A. and Noonan G.E. 2009b. Monitoring of a secondary recovery application of leachate injection into a heap. *Hydrometallurgy* **99**, 238–248

Rucker D.F. and Noonan G.E. 2013. Using marine resistivity to map geotechnical properties: A case study in support of dredging the Panama Canal. *Near Surface Geophysics* **11**(6). doi:10.3997/1873-0604.2012017

Sasaki Y. 1994. 3-D resistivity inversion using the finite element method. *Geophysics* **59**, 1839–1848.

Singha K. and Gorelick S.M. 2006. Effects of spatially variable resolution on field-scale estimates of tracer concentration from electrical inversions using Archie's law. *Geophysics* **71**, G83–G91.

Spitzer K., Chouteau M. and Boulanger O. 1999. Grid-independent electrode positioning for 3D DC and IP forward modeling. *Proceedings of the 2nd International Symposium on 3D Electromagnetics*, 189–192.

Wilkinson P.B., Chambers J.E., Meldrum P.I., Ogilvy R.D. and Caunt S. 2006. Optimization of array configurations and panel combinations for the detection and imaging of abandoned mineshafts using 3D cross-hole electrical resistivity tomography. *Journal of Environmental and Engineering Geophysics* **11**, 213–221.

Zhou B. and Dahlin T. 2003. Properties and effects of measurement errors on 2D resistivity imaging surveying. *Near Surface Geophysics* **1**, 105–117.

Zhou B. and Greenhalgh S.A. 2001. Finite element three-dimensional direct current resistivity modelling: Accuracy and efficiency considerations. *Geophysical Journal International* **145**, 679–688.